ADVANCING EARTH AND SPACE SCIENCE

JGR Space Physics

RESEARCH ARTICLE

10.1029/2022JA030644

An Imaging Evidence of the East Wall Structuring of Eastward Drifting Depletions Observed Near the EIA Crest in India

Saranya Padincharapad[1,2], Navin Parihar[3], Alok Taori[4], and Samireddipalle Sripathi[3]

[1]Equatorial Geophysical Research Laboratory, Indian Institute of Geomagnetism, Tirunelveli, India, [2]Manonmaniam Sundaranar University, Tirunelveli, India, [3]Indian Institute of Geomagnetism, Navi Mumbai, India, [4]National Remote Sensing Centre, Hyderabad, India

Key Points:

- Rare observations of the structuring on the east wall of an eastward drifting depletion
- Secondary depletion that grew on the primary depletion also showed the east wall structuring
- Supports Zalesak et al. (1982, https://doi.org/10.1029/JA087iA01p00151) simulations that secondary instabilities can grow on east wall of a westward tilted depletion

Correspondence to:

N. Parihar,
navindeparihar@gmail.com

Citation:

Padincharapad, S., Parihar, N., Taori, A., & Sripathi, S. (2022). An imaging evidence of the east wall structuring of eastward drifting depletions observed near the EIA crest in India. *Journal of Geophysical Research: Space Physics*, *127*, e2022JA030644. https://doi.org/10.1029/2022JA030644

Received 11 MAY 2022
Accepted 22 SEP 2022

Author Contributions:

Conceptualization: Navin Parihar
Data curation: Navin Parihar
Formal analysis: Saranya Padincharapad
Investigation: Saranya Padincharapad, Navin Parihar
Supervision: Navin Parihar, Alok Taori, Samireddipalle Sripathi
Writing – original draft: Saranya Padincharapad, Navin Parihar
Writing – review & editing: Saranya Padincharapad, Navin Parihar, Alok Taori, Samireddipalle Sripathi

Abstract Structuring on the west (east) wall of eastward (westward) drifting airglow depletion under quiet (storm) time is common. Here, we report for the first time the rare occurrence of the east wall structuring of an eastward drifting depletion near the crest of equatorial ionization anomaly (EIA) in India on 16 April 2012 under quiet geomagnetic conditions. We observed a linear depletion having a westward tilt of ∼25° and eastward drift speed of ∼129 m/s in the beginning. First prominent structuring occurred on its west wall that later swiftly surged poleward within next 6–12 min and bifurcated, that is, behaved like a secondary depletion growing on the primary one. Second west wall structuring then occurred but had considerably subdued growth. Meanwhile, main depletion bent slightly eastward above its branching node, and two structuring appeared on the east wall in succession. Secondary depletion then slightly contracted equatorward, and structuring emerged from its east wall, too, that later stretched eastward, got linked with main depletion and formed *grid mesh* shaped feature. Second structuring on the west wall started fading; while, those on the east wall swiftly evolved, surged poleward and gained prominence. Also, their westward tilt decreased. During the occurrence of these events, gravity waves (GWs) and the retreat of EIA were active overhead. Current study serves as first imaging evidence of Zalesak et al. (1982, https://doi.org/10.1029/JA087iA01p00151) simulations that the east wall of a westward tilted depletion can become unstable and host secondary instabilities. Possibly these structuring were excited by GWs via Rayleigh-Taylor instability.

Plain Language Summary Generally the west (east) wall of eastward (westward) drifting airglow depletion is unstable to eastward (westward) drifts and hosts secondary instabilities (SIs). Present study features the rare occurrences of their growth on the east wall of an eastward drifting depletion. Concerned depletion was linear in the beginning and had a significant westward tilt; however, several structuring developed on both its walls as it drifted eastward. First prominent one occurred on its west wall that later swiftly surged poleward and bifurcated like usual depletion, that is, was like a secondary depletion. Second west wall structuring followed this one but had considerably subdued growth. Simultaneously, main depletion bent slightly eastward above its branching node and two structuring appeared on the east wall in succession. Secondary depletion then, too, developed structuring on its east wall that later extended eastward and got linked with main depletion. Second west wall structuring later disappeared; while, those on the east wall swiftly evolved, surged poleward and gained prominence. During the occurrence of these events, gravity waves and the retreat of equatorial ionization anomaly were active overhead. Current observations show that the east wall of a westward tilted depletion can become unstable and host SIs.

1. Introduction

Often secondary instabilities (SIs) are seen to develop on the walls of nonlinearly growing equatorial plasma bubbles (EPBs) (Hysell, 2000; Huba & Joyce, 2007; Li et al., 2021; Muralikrishna & Vieira, 2007; Zalesak et al., 1982). Numerous radar and optical airglow observations from the Northern Hemisphere have shown their development on the west wall of an eastward drifting depletion (EDD) (Kelley et al., 2000; Makela, 2006; Mukherjee, 2003; Mendillo & Baumgardner, 1982; Rodrigues et al., 2018; Rohrbaugh et al., 1989; Tsunoda, 1983, 2015; Tsunoda & White, 1981; Tsunoda et al., 1982, 2011; Xiong et al., 2018; Yokoyama et al., 2014, 2015). These studies indicate that the west wall of an EDD is more unstable than the east one under the influence of an eastward blowing neutral wind and thus, is more favorable for the development of SIs. Kelley (2009) and Makela, Kelley, et al. (2006) have elaborately discussed conditions for their growth, viz., $(\mathbf{E}' \times \mathbf{B}).\nabla n > 0$ (where the terms have their usual meaning). Mukherjee (2003) and Tsunoda et al. (2011) have reported their occurrences on the west

10.1029/2022JA030644

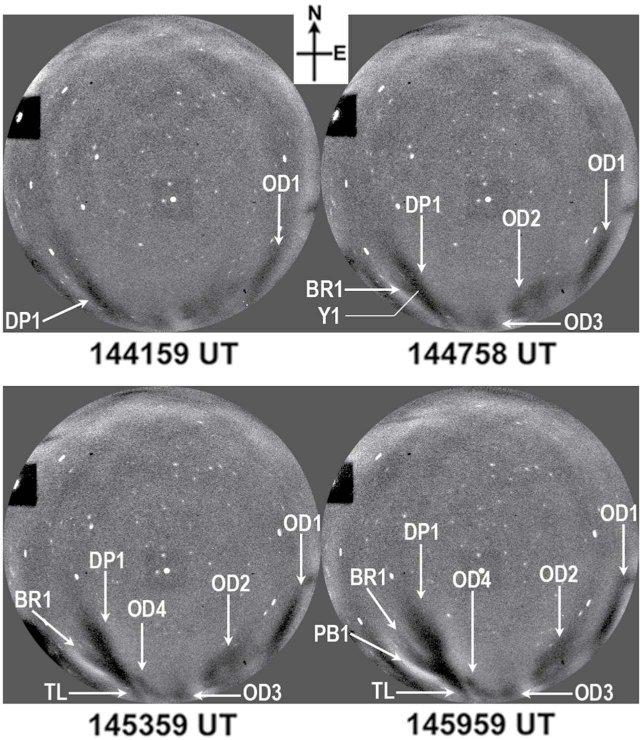

Figure 1. All-sky imager 630 nm nightglow images showing different depletions observed during 14:42–15:00 UT (2012–2030 IST). Time stamp information is in ***hhmmss*** format. DP1 is the prominent depletion that showed structuring on both the walls. First branching that emerged on its west wall is BR1 and Y1 is the branching node. Plasma blob that developed adjacent to BR1-DP1 is PB1. Other depletions seen in the field-of-view are OD1, OD2, OD3 and OD4. TL is the equatorward extending thin depleted tendril of DP1.

wall of depletions in the Asian sector. Conjugate stations imaging observations of airglow depletions also showed their development on the west wall (Otsuka et al., 2002; Shiokawa et al., 2004).

However, limited reports exist in literature that feature imaging observations of their growth on the east wall mainly under geomagnetic storm conditions (Garcia et al., 2000; Makela et al., 2006b; Martinis et al., 2009). During the geomagnetic storm of 22 and 23 November 1997, Garcia et al. (2000) reported depletion over Arecibo in Puerto Rico wherein the plume-like features developed on the east wall. Makela, Kelley, et al. (2006) reported SIs on the east wall of a westward drifting depletion (WDD) over Haleakala Volcano in Hawaii during the progression of a minor geomagnetic storm. Martinis et al. (2009) reported depletion over Arecibo that reversed its drift from eastward to westward and then, the finger-like features developed on its east wall. In all these reports, the structuring was seen on the east wall of the WDD. In contrast, airglow imaging observations from the Southern Hemisphere have shown a complex picture of the development of depletions wherein both primary and secondary depletions appear together in highly structured form (sometimes indistinguishable) (Abalde et al., 2001; Martinis et al., 2006, 2018; Pimenta et al., 2003; Sahai et al., 2006, 2009). Such differences in the growth of SIs in two hemispheres in the American sector might arise due to either different morphology of the geomagnetic field lines or the prevalent South Atlantic Anomaly or both and is the subject of another investigation (see Martinis and Mendillo, 2007).

Ranchi (23.3°N, 85.3°E, mlat. ~19°N) is located near the crest of equatorial ionization anomaly (EIA) in India and is comfortably positioned to image EPBs having the apex height in the range of ~300–1,600 km. In this paper, we present rare observations of the growth of SIs on both the walls of an EDD over Ranchi in India under quiet geomagnetic conditions on 16 April 2012. During its occurrence, the backward movement of EIA toward the equator was active overhead and associated depletion was embedded in its plasma. We discuss the possible underlying mechanisms behind their development when the EIA retreat was active.

2. Instrumentation and Data

A six-filter all-sky imager (ASI) was deployed at Ranchi for campaign-mode nightglow observations during April 2012. The details of this ASI can be found in Parihar et al. (2017). A narrowband optical filter (central wavelength ~630 nm, bandwidth ~2.2 nm and transparency ~77%) was used to monitor atomic oxygen red line emission. Rest of the five filter slots were used to monitor OI 557.7 nm, P_1 (2) and P_1 (4) lines of OH (6, 2) Meinel band, OH broadband emissions from the mesosphere-lower thermosphere region and the background at 857 nm. Each emission was monitored for 60 s that resulted in a cycle-time of 6 min. Image processing and limitations with the intensity calibration has been discussed elsewhere (Parihar, 2019). Quiet geomagnetic conditions prevailed on 16 April 2012 ($Kp < 2$, $Ap = 4$ and Dst varied from -4 *to* 10 nT).

3. Observations

Since the beginning of airglow imaging at ~14:36 Universal Time (UT) on 16 April 2012, several EDDs were seen in the field-of-view (FOV). It is worth mentioning here that *Indian Standard Time, IST = UT* + 0530 ≈ *LT, Local Time*. Figures 1–3 present their evolution during 14:42–15:00, 15:06–15:24, and 15:30–15:48 UT, respectively. Prominent depletion of our interest that showed the structuring on its east wall is hereafter referred to as DP1 and can be seen in the south-western sector of the FOV in Figure 1. Remaining depletions (marked as OD1, OD2, OD3, OD4, OD5, OD6, and OD7 in Figures 1–3) were rather faint and had smaller north-south (NS) scale size, varied in contrast and were limited to the southern sector of the FOV. Depletions OD1, OD2, OD3 and

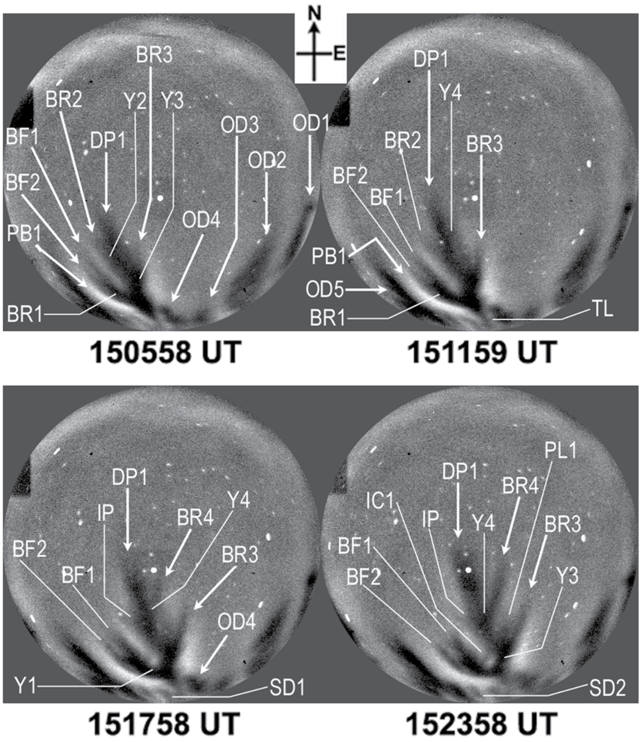

Figure 2. Same as Figure 1 but for 15:06–15:24 UT (2036–2054 IST). BR2 is the second west wall branching of DP1 that evolved after BR 1 from the node Y2. BF1 and BF2 are the bifurcations of BR1. BR3 and BR4 are the east wall branching of DP1 that successively developed from the node Y3 and Y4, respectively. IP is the inflection point where the bending of DP1 occurred. PL1 is the plume-like feature close to BR3. IC1 is the first interconnection channel between BR1 and DP1. SD1, SD2 and OD5 are the depletions that succeeded DP1.

OD4 preceded DP1; while, OD5, OD6 and OD7 succeeded it. Concurrently, the EIA retreat toward the equator was in progression over Ranchi and is presented in Appendix A.

DP1 initially appeared as a single linear depletion during 14:36–14:42 UT (the upper panel in Figure 1). However, the successive images showed that its southern fraction was like a *thin depleted tendril* (termed as TL) that extended toward the equator and was flanked on its east by another depletion OD4. Apex height of depletion DP1 was ∼570 km at 14:48 UT. About this time, a branching (hereafter referred to as BR1) emerged out from its west wall, and its branching node (termed as Y1) was located at ∼160 km below the main apex. Such west wall branching of airglow depletions has been commonly reported (Kelley et al., 2000; Makela, 2006; Mukherjee, 2003; Mendillo & Baumgardner, 1982; Mendillo & Tyler, 1983; Rohrbaugh et al., 1989; Xiong et al., 2018), and is due to the presence of steep density gradient therein which provides favorable conditions for the excitation of SIs (Huang & Kelley, 1996; Mendillo & Tyler, 1983). Concurrently, airglow enhancement occurred in the adjoining regions of both the walls. When compared, the enhancement near the west wall was more than that near the east wall. Next, during 14:54–15:06 UT, the structuring BR1 surged poleward and then bifurcated like usual airglow depletion (see the bottom panel in Figure 1 and upper panel in Figure 2); hence, can be referred to as a secondary depletion that grew on the primary one. We name these bifurcations as BF1 and BF2. Also, airglow enhancement near its west wall increased and a well-marked plasma blob (hereafter referred to as PB1) was evident. Plasma blobs are the regions of significantly enhanced plasma density than that of the ambient ionosphere and are formed by the re-enhancement of localized eastward polarization field inside an EPB (Kil et al., 2011; Krall et al., 2010; Le et al., 2003; Park et al., 2008; Pimenta et al., 2007; Wang et al., 2019; Yokoyama et al., 2007). At 15:06 UT, the apex height of depletion DP1 was ∼700 km and the second branching (hereafter referred to as BR2) appeared on its west wall. We found its branching node (termed as Y2) to be located at ∼100 and ∼159 km, respectively, from the main apex and the branching node Y1 of BR1. Also, depletion DP1 along with its branching showed a westward tilt of ∼25 ± 1°. Such westward tilt of depletions arises due to the integrated effect of the shear in zonal plasma drift set up by Pedersen conductivities in the equatorial F-region and off-equatorial E-region (Makela, 2006; Mendillo & Tyler, 1983; Zalesak et al., 1982).

During 15:06–15:12 UT (the upper panel in Figure 2), we found two structuring to appear on the east wall of depletion DP1. First branching (hereafter referred to as BR3) developed at ∼15:06 UT and its node (termed as Y3) was located at ∼196 km from the main apex. A little later (∼15:12 UT), second structuring (hereafter referred to as BR4) appeared at ∼68 km from the main apex and ∼134 km from the branching node Y3 of BR3. We mark its branching node as Y4 in Figure 2. Such branching on the east wall are rare in the imaging observations from the Northern hemisphere and have been reported by Garcia et al. (2000), Makela, Kelley, et al. (2006) and Martinis et al. (2009). Unlike the present observations for an EDD under quiet geomagnetic conditions, these investigators observed such east wall branching on a WDD under geomagnetic storm conditions. The presence of the branching BR3 and BR4 on the east wall of depletion DP1 suggests that its east wall was unstable enough to host SIs (Huang & Kelley, 1996; Mendillo & Tyler, 1983). On the west, blob PB1 continued to intensify and attained its maximum at 15:12 UT. Also, the branching BR1 was well-developed and had a scale size of ∼233 ± 6 km; while, the branching BR2 showed relatively small growth and its scale-size was limited to ∼36 ± 6 km. We also found that the bifurcations BF1 and BF2 of the branching BR1 were distinct and well-developed (having scale-size of ∼84 ± 18 km and 90 ± 17 km, respectively). Also, depletion DP1 appeared to be slightly bent toward the east above the branching node Y2 of BR2 (clearly seen at 15:18 UT in the lower panel in Figure 2). We term this inflection point as IP (the lower panel in Figure 2). Such eastward bending of depletion DP1 clearly points toward an increase in eastward plasma drift with increasing latitude beyond this inflection point and has been elaborated

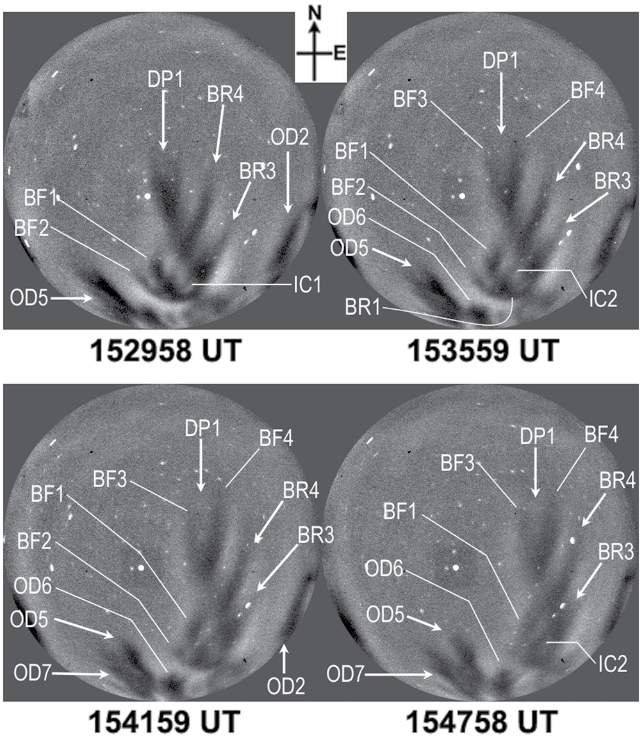

Figure 3. Same as Figures 1 and 2 but for 15:06–15:24 UT (2100–2118 IST). BF3 and BF4 are the bifurcations of DP1. After IC1, IC2 is the second interconnecting channel between BR1 and DP1. Together IC1, IC2 and the eastward tilted BF1 form a grid mesh-shaped depleted feature between BR1 and the lower half of DP1 at around 15:36 UT. OD6 and OD7 are two depletions that segregated from the east and west of OD5.

in the discussion section. Beyond 15:12 UT, the west and east wall showed contrasting behavior. On the west, the branching BR2 started fading in the background; while, the branching BR3 and BR4 on the east swiftly evolved, extended poleward and gained visibility.

During 15:18–15:24 UT (the lower panel in Figure 2), the branching BR1 together with its bifurcations slightly contracted toward the equator, and some airglow enhancement occurred in the region between its east wall and the west wall of depletion DP1. About this time, their spacing was ∼64 ± 6 km. Some structuring occurred on both the walls of bifurcation BF1. Just above the branching node Y1 of BR1, we observed one such thin and faint structuring that stretched from its east wall to the west wall of depletion DP1 so as to form an interconnecting channel (termed as IC1; see image at 15:24 UT in Figure 2). An irregular bulge was evident on its west wall. Also, we observed unclear signs of the bifurcation of its apex (seen as broadening). Bifurcation BF2 appeared to separate out from the branching BR1 so as to form a linear isolated depletion. Meanwhile, the apex of depletion DP1 broadened. We also observed a plume-like feature (termed as PL1) to develop on its east wall near the branching node Y3 of BR3. A significant fraction of this plume PL1 appeared to be merged with that of the branching BR3; however, its apex was distinct (see the lower panel in Figure 2). Along with the branching BR3 and BR4, its presence on the east wall ascertains that the east wall of depletion DP1 was unstable (Huang & Kelley, 1996). Also, the apex of the branching BR4 almost reached that of depletion DP1 (∼780 km) and its branching node Y4 was located near the shallow inflection point IP where the bending of depletion DP1 occurred. Starting 1524 UT, the bottommost fraction of depletion DP1 along with its tendril TL began to disappear in the background. As a consequence, the east wall branching BR1, the base of depletion DP1 and the west wall branching BR3 together outlined a *cusp-shaped depleted arc* (shown as A1 in Figure B1 of Appendix B). We also observed two small-scale faint depletions (termed SD1 and SD2) near the southern edge of the FOV that succeeded depletion DP1.

At 15:30 UT (the upper panel in Figure 3), the apex of the bifurcation BF1 tilted considerably to the east and almost extended to the west wall of depletion DP1. Although thin and faint, its east wall structuring were more evident, and two of them can be seen to stretch toward the west wall of depletion DP1. Again, the irregular bulge on its west wall appeared to connect it with the bifurcation BF2 which was more distinct now. Also, the main apex of depletion DP1 bifurcated and surged poleward. We name its bifurcations as BF3 and BF4 in Figure 3. We found the bifurcation to occur at ∼770 ± 14 km which is in good agreement with that reported by Mendillo and Tyler (1983). They studied the geometry of airglow depletions over Ascension Island and found that they occurred generally at 740 ± 10 km. Such bifurcation can be explained in terms of inhomogeneous electric field present within the bubble. Numerical simulations by Huang and Kelley (1996) indicate that an inhomogeneous electric field inside the bubble drives the charged particles to both its walls which then results in its bifurcation. Also, considerably disappeared tendril TL merged with the apex of depletion OD4 on its east and with that of small depletion SD1 on its west so as to form an arch-shaped depletion (termed as A2 in Figure B1 of Appendix B). Starting 15:30 UT, the westward tilt of depletion DP1 along with its structuring began to decrease and disappear in the background. At 15:36 UT, the tilted apex of bifurcation BF1 almost appeared detached from the branching BR1 so as to form an isolated structure. This detached tilted apex together with the branching BR1 and two interconnecting channels IC1 and IC2 formed a *grid mesh-shaped* feature with the lower fraction of depletion DP1 (termed as G1 in Figure B1 of Appendix B). The westward tilt of depletion DP1 further decreased and the branching BR3 and BR4 on its east wall stretched toward the pole.

During 15:42–15:48 UT (the lower panel in Figure 3), depletion DP1 was nearly NS aligned. Also, the branching BR3 and BR4 and the bifurcations BF3 and BF4 were well-developed. The branching BR3 and BR4 had a scale size of ∼180 ± 25 km and 156 ± 12 km, respectively; while, that of the bifurcations BF3 and BF4 was

10.1029/2022JA030644

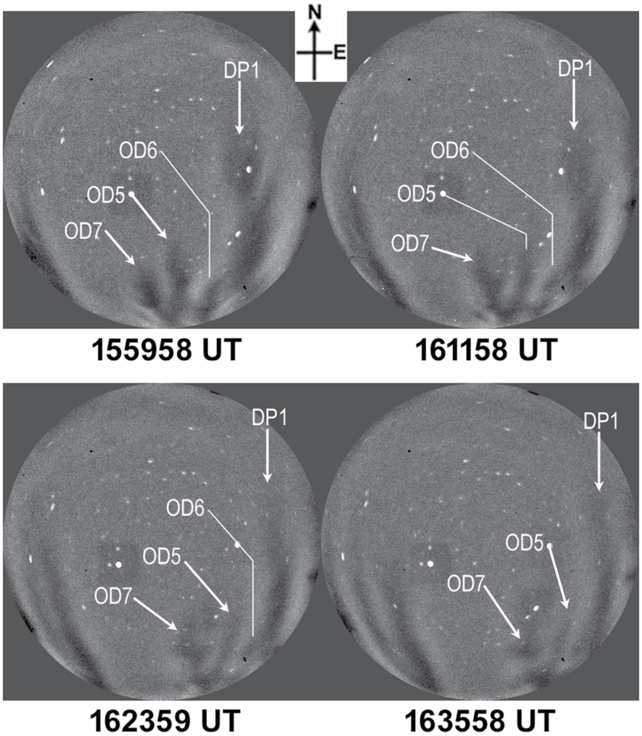

Figure 4. Selected all-sky imager images during 16:00–16:36 UT showing the disappearance of different structuring and bifurcations that lead to the formation of a linear depletion DP1.

~124 ± 6 km and 179 ± 5 km, respectively. Shiokawa et al. (2004) have reported the scale size of bifurcating features to be ~50 km. With the further disappearance of depletion DP1 and associated features, the bifurcations BF3 and BF4 together formed an isolated V-shaped depletion. Also, the detached apex of the bifurcation BF1 extended toward depletion DP1 and was finally located between the branching BR4 and bifurcation BF4. Still, the *grid mesh-shaped* feature, G1, was apparent.

Finally, selected ASI images depicting the subsequent development taking place in the FOV are shown in Figure 4. Secondary depletions/structuring and bifurcations continued to disappear further which resulted in the formation of a single linear NS aligned depletion at ~16:24–16:30 UT.

Similar to depletion DP1, depletion OD5 initially appeared to be a single linear depletion till 15:18–15:24 UT (the lower panel in Figure 2). Successive images showed that two depletions separated out on both its east and west. On its east, relatively small scale size depletion preceded it near the equatorward edge during 15:30–15:48 UT (marked as depletion OD6 in Figures 3 and 4). Simultaneously, another depletion of similar scale size segregated from its west wall and was clearly distinguishable at 15:48 UT (marked as depletion OD7 in Figures 3 and 4). Depletions OD5, OD6, and OD7 also showed similar structuring or irregular bulging or plume-like features on their walls.

4. Discussion

We present the complex evolution of the structuring on the walls of depletions that were recorded in airglow imaging at Ranchi (mlat. ~19°N) on 16 April 2012. Since the start of imaging, a prominent depletion DP1 (having a westward tilt of ~23 ± 2° and eastward drift speed of ~128–149 m/s) was seen. A plot of its drift speed versus time is shown in Figure 5d. During its progression, the retreat of EIA was active overhead. It is known that steep electron density gradients on the walls of nonlinearly rising EPBs are more favorable for the growth of SIs. As depletion DP1 traversed eastward through the FOV, SIs (seen as several structuring) are developed on its walls. First prominent one, the branching BR1 occurred on its west wall at ~14:48 UT. Within the next 6–12 min, the branching BR1 swiftly extended poleward and bifurcated like a usual depletion. As such, the branching BR1 can be considered as a secondary depletion growing on the wall of the primary depletion. Second structuring BR2 occurred on the west wall at 15:06 UT; however, it was not as prominent as the branching BR1. Generally, steep density gradient exists on the west wall of an EDD in comparison to the east one (Mendillo & Baumgardner, 1982; Pimenta et al., 2003). West wall structuring of EDD DP1 suggests that the neutral wind was eastward. We looked into Horizontal Wind Model (HWM) estimates to understand the winds in the F-region and found an eastward zonal wind of speed ~49–94 m/s. Usual west wall structuring of an EDD in the post-sunset hours has been explained in terms of an eastward neutral wind driven gradient-drift instability (GDI) (Tsunoda, 1983, 2015; Tsunoda et al., 2011; Yokoyama et al., 2014, 2015).

While depletion DP1 continued to drift eastward, two structuring BR3 and BR4 developed on its east wall during 15:06–15:12 UT that later gained prominence and surged poleward. Simultaneously, thin and faint structuring occurred in the east wall of branching BR1 that later stretched toward depletion DP1 and formed the interconnecting channels IC1 and IC2. Makela, Kelley, et al. (2006) reported the structuring on the east wall of a WDD over Haleakala Volcano in Hawaii during a minor geomagnetic storm of 4 February 2003. Authors explained their occurrences on the basis of the wind-driven GDI as: for the northeast directed density gradient, the east wall can become unstable for an electric field with an eastward or equatorward component or a wind with a westward or equatorward component. This indicates a westward wind is required to explain the growth of the branching BR3 and BR4 via wind-driven GDI. However, both imaging observations and HWM estimates show that neutral wind was eastward in our case. This poses question like what could be the reason for the east wall structuring in our case.

10.1029/2022JA030644

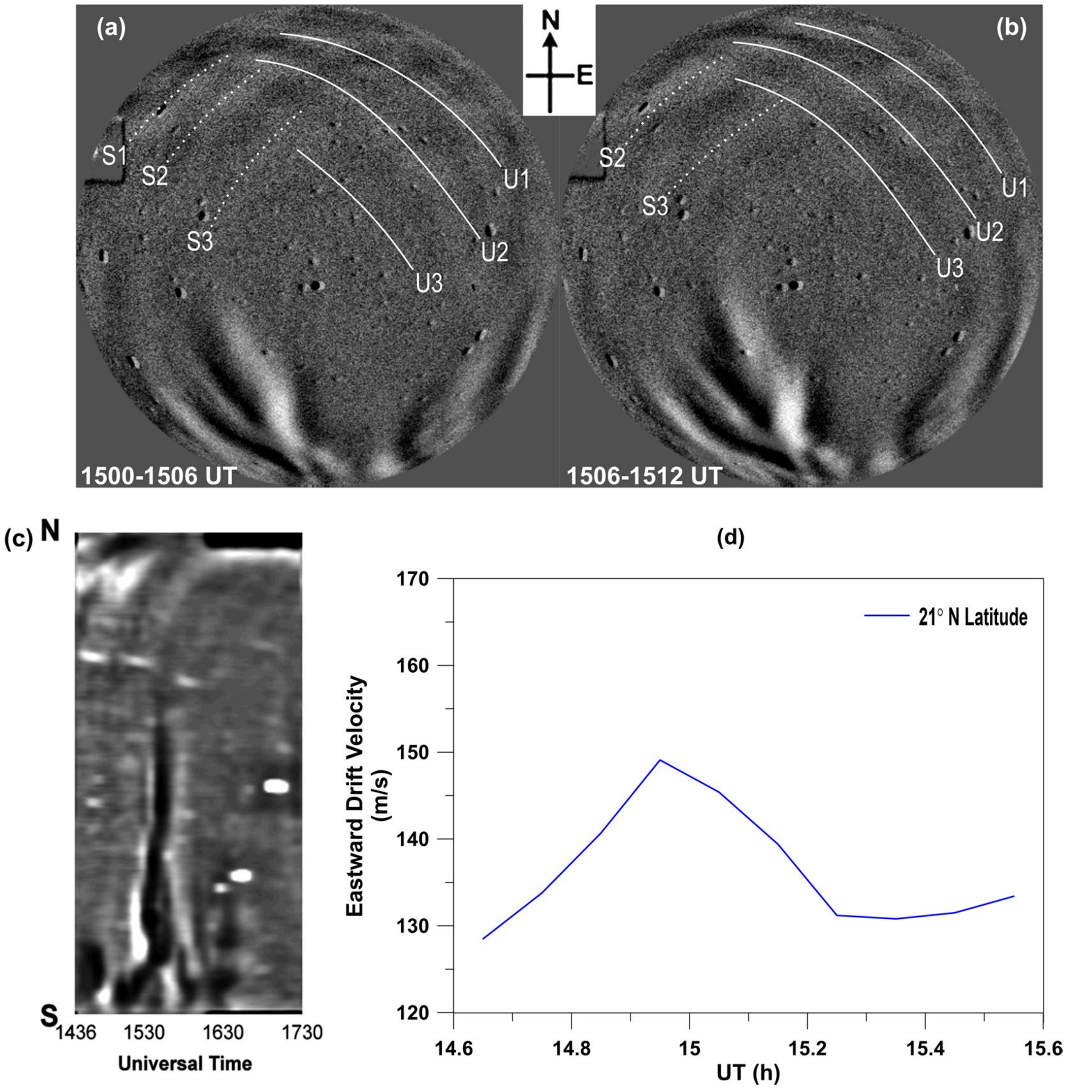

Figure 5. (a–b) Time difference images during 15:00–15:12 UT showing the gravity waves activity near the north horizon. Well-marked fronts are named as S1, S2, S3, U1, U2 and U3. S- and U- marked wave fronts propagated in SE-NW and SW-NE directions, respectively. (c) North-south keogram (generated using images during 14:36–17:30 UT) showing two northward propagating wave fronts during 14:36–16:00 UT. (d) Plot of the eastward drift speed of depletion DP1 versus time during 14:36–15:36 UT. An increase in drift from 129 m/s to 149 m/s was seen just before the east wall structuring occurred.

Mendillo and Tyler (1983) suggested that the sharp density gradients can develop on the east wall of a westward tilted depletion which can then become unstable and host SIs. Zalesak et al. (1982) studied the effects of an eastward neutral wind on the evolution of EPBs by taking the Pedersen conductivity into account in both the F-region near the equator and the E-region in higher-latitudes. Authors found that the west wall of a vertical or non-tilted EPB is subject to SIs in the presence of an eastward neutral wind; however, for an EPB with a westward tilt, its east wall can be unstable to gravitational RT instability. We found that depletion DP1 had a westward tilt of ~25–26° when the east wall structuring occurred during 15:06–15:12 UT. The westward tilt of depletions has been explained in terms of the shear in zonal plasma drift set up by the ratio of Pedersen conductivities in the equatorial F- and off-equatorial E–region. At the equator, the vertical polarization electric field driven by the zonal neutral wind is partially "shorted out" by the background E-region conductivity, causing a relative motion between the plasma and the neutral wind. This produces vertical shear in the plasma motion even though there is no vertical shear in the zonal neutral wind. This shear is mainly responsible for "C" shaped radar maps. Supported by Zalesak et al. (1982) and Mendillo and Tyler (1983) interpretations, we believe that considerable westward

10.1029/2022JA030644

tilt seen in the present observations might be one of the causes for the east wall to become unstable and host SIs. Zalesak et al. (1982) further suggested that SIs can occur on the west wall at lower altitudes but they can grow on the east wall at higher altitudes and this "switching" takes place at about 370 km. Wind driven GDI dominates at lower altitudes; while, gravitational RT instability is favorable mechanism at higher altitudes. We found this "switching" height between the branching node Y1 and Y3 to be ~490 km. Possibly SIs on the east wall occurred under gravitational RT instability.

Gravity waves (GWs) are well-known for aligning/modulating the ionospheric plasma distribution (Fejer & Kelley, 1980; Kelley et al., 1981; and citations to the article). When the structuring occurred, faint signatures of GWs ($\lambda_H \sim 147$–234 km) were seen in airglow images wherein their fronts propagated in S-N, SE-NW, and SW-NE directions. Figures 5a and 5b presents the time difference images during 15:00–15:12 UT wherein GWs fronts can be seen near the north horizon. North-south keogram (shown in Figure 5c) clearly showed wave fronts that propagated northward. Possibly due to the bright EIA structure, these wave fronts were not apparent in the southern sector. Interestingly, GWs wavelengths reasonably matched with the internode spacing between two related structuring on each wall (which lay in the range of 134–159 km). Using numerical simulations, Huang and Kelley (1996) studied the effect of both large-scale and small-scale GWs on the RT instability. Simulations indicate that (a) large-scale GWs seed the RT instability and determine the external dimensions of irregularities, and (b) smaller-scale GWs results in multiple plumes on the unstable wall. Possibly these GWs acted on unstable walls of depletion DP1 and excited SIs via RT instability or GWs driven GDI (Fejer & Kelley, 1980; Kagan & Kelley, 1998). We also found an increase in the drift velocity of depletion DP1 from 129 m/s to 149 m/s before the occurrence of the east wall structuring (see Figure 5d). As the shear in plasma flow directly influences the density protrusions, their presence can have a dramatic impact on the RT instability. Satyanarayana et al. (1984) suggested that the variation of maximum growth rate of RT instability with the wavelength depends upon the strength of the velocity shear. Similarly, Guzdar et al. (1982) showed that the presence of velocity shear can suppress or preferentially excite the growth rate of instability depending upon the factor kL (where k is the wavenumber of horizontal perturbation and L is the scale length of the background electron density perturbations). When $kL > 1$ (i.e., for the short-wavelengths), the growth rate of RT instability is reduced; whereas, it maximizes for $kL < 1$ (i.e., for the long wavelength regime). We found the spatial scale of SIs on both the walls to be ~15–25 km in the initial stage of their development. Using this information (i.e., assuming $L \sim 15$–25 km) and $\lambda_H \sim 147$–234 km, we found kL to be in the range of 0.40–1.07. As such, these persistent GWs can excite the SIs in accordance with Guzdar et al. (1982) observations.

Numerical simulations on the impact of diffusion on the EPBs evolution by Huba and Joyce (2007) suggest that numerous bifurcations and SIs can grow on their walls. Herein, the EIA retreat was active overhead and depletion DP1 was embedded in its relatively much denser plasma. As such, diffusion of ambient plasma across its walls is possible. In accordance with Huba and Joyce (2007) simulations, such diffusion can result in its complex evolution with multiple bifurcations on both its walls. Muralikrishna and Vieira (2007) also suggest that the cascade process linked with the large-scale upwellings could generate SIs via cross-field instability and GDI. Studies by Garcia et al. (2000) and Kelley et al. (2004) indicate that favorable conditions are set for the $E \times B$ instability when sharp plasma density gradients exist near the edges of primary depletion, and SIs can grow on their walls. Garcia et al. (2000) reported the evolution of plumes on the east wall driven by this instability. Authors first observed airglow intensification near the east edge of depletion that resulted in a very sharp gradient of emission strength and then plume-like structures developed therein. Present case is somewhat akin to their observations. Herein, depletion DP1 was embedded in intense plasma of the EIA retreat. Due to the EIA retreat, sharp density gradients possibly developed at higher altitudes and higher electron density on the east wall could have provided a favorable condition for the growth of SIs in accordance with the simulation results of Zalesak et al. (1982). The occurrence of blobs nearby depletion DP1 lends support to this notion.

Adjacent to the west wall of branching BR1, plasma blob PB1 was seen during 14:48–15:18 UT. Simultaneously, comparatively weaker airglow enhancement also occurred near the east wall branching BR3. Several investigators have reported their observations near the EIA crest regions (Kil et al., 2011; Krall et al., 2010; Le et al., 2003; Park et al., 2008; Pimenta et al., 2007; Wang et al., 2019; Yokoyama et al., 2007). Authors suggest that the re-enhancement of localized eastward polarization field present within the irregularity itself

10.1029/2022JA030644

produces these blobs. Studies by Le et al. (2003) and Pimenta et al. (2007) indicate that they usually develop during the westward electric field conditions or when the reversal from eastward to westward electric field occurs. In the present study, the blob PB1 occurred at ∼2½ hours after local sunset. Usually they occur within about 3 hr after sunset near the EIA crest regions (Le et al., 2003). We also noted a few instances of detachment of depleted features from the primary feature during 15:24–15:48 UT. First, the bifurcation BF2 got detached from the branching BR1 at 15:24 UT. Next, depletion DP1 along with its structuring appeared like an isolated feature that rested on depleted arch A2. Also, the bifurcations BF3 and BF4 together formed an isolated V-shaped depletion at 15:42–15:48 UT. Previously, Sahai et al. (2006) reported the occurrences of such detachment associated with airglow depletions in Brazil under both geomagnetic quiet and disturbed conditions. Authors suggest that the presence of non-uniform vertical plasma drift due to inhomogeneous zonal electric field can result in one fraction moving faster or slower than other which consequently results in detachment.

5. Summary and Conclusions

The growth of SIs on the west wall of an EDD is common; however, those on its east wall are rare. Present study features their complex evolution on both the walls of an EDD that was recorded in OI 630 nm nightglow imaging over Ranchi (mlat. 19°N) in India on 16 April 2012. Such simultaneous occurrence of the structuring on both walls makes the current observations interesting. Salient features of the present study are as followings:

1. Since 14:36 UT, a linear depletion DP1 that drifted eastward ($\upsilon \sim 129$ m/s) and had a westward tilt ($\theta \sim 25°$) was seen. As it drifted eastward, SIs developed subsequently on both its walls (seen as several structuring) and the bifurcation of apex of both main and secondary depletion occurred. During its progression, the EIA retreat was active overhead.
2. First prominent branching BR1 emerged out from its west wall at 14:48 UT, and then surged poleward and bifurcated like usual airglow depletion within the next 6–12 min. Simultaneously, a well-marked plasma blob PB1 developed on its west wall. The second west wall branching BR2 then appeared at 15:06 UT, however, was not prominent as BR1 and showed subdued growth.
3. Next, two structuring BR3 and BR4 emerged in succession on its east wall during 15:06–15:12 UT. About this time, depletion DP1 appeared to be slightly bent eastward above the branching node Y2 of BR2. Beyond 15:12 UT, contrasting behavior of its west and east wall was seen. On the west wall, the branching BR2 started fading and almost disappeared at 15:24 UT. When branching BR1 along with its bifurcations slightly contracted toward the equator, thin but faint structuring IC1 and IC2 emerged on its east wall that stretched eastward, and then got linked with depletion DP1 and formed *grid mesh* shaped feature at 15:36 UT. Meanwhile, the branching BR3 and BR4 on the east wall swiftly evolved, extended poleward, and gained visibility. Beyond 15:30 UT, the apex of depletion DP1 bifurcated, its westward tilt started decreasing and it began to disappear in the background. The depletion DP1 was nearly NS aligned during 15:42–15:48 UT and its bifurcations as well as the east wall branching were well-developed.
4. An eastward neutral wind driven GDI (Tsunoda, 1983, 2015; Tsunoda et al., 2011; Yokoyama et al., 2014, 2015) can explain the west wall structuring; however, not the east one. Zalesak et al. (1982) simulations suggest that the east wall of a topside bubble or westward tilted depletion can become unstable. Possibly this appears to be the case here wherein depletion DP1 showed a significant westward tilt of ∼25° when these east wall structuring occurred. Since no geomagnetic storm or westward zonal neutral winds was noticed on this day, we believe that this westward tilt could be one of the reasons for the east wall structuring. Another reason could be GW activity which persisted during the progression of this event might have possibly triggered their excitation via Rayleigh-Taylor instability and then SIs developed on the east wall. While these results are interpreted based on a single event, we are looking for additional resources to understand further about these east wall structuring.

Such formation of structuring on both the walls of airglow depletion upon its interaction with the EIA retreating plasma is novel and demands more understanding.

Appendix A: Signatures of the EIA Retreat Over Ranchi

Figure A1a presents OI 630 nm emission intensity variations at ~23.3°N (corresponding to zenith) and two sample locations at 22.2°N and 21.6°N during 14:36–18:30 UT (which corresponds to the period between the post-sunset hours and midnight). We observe an unclear elevated peak in the intensity variations over 23.3°N during 14:36–15:00 hr. At lower latitudes (21.6–22.2°N), the intensity variations clearly show an elevated hump at ~15:18 UT. Such an equatorward moving peak in the intensity variation is often present during the post-sunset hours and midnight hours over these latitudes and is a manifestation of the EIA retreat toward the equator/low-latitude during night (Parihar, 2019; Parihar et al., 2018; Rastogi & Klobuchar, 1990; Sridharan et al., 1993). As the EIA moves into the FOV, an increased ionization results in more recombination thereby leading to an increase of intensity. When the EIA is overhead, a maximum in intensity is seen, and is followed by a decrease as it recedes away from the FOV. As an example, Parihar (2019) reported a usual evening decrease of intensity till 13:48 UT followed by the EIA associated hump during 13:48–16:00 UT on 3 January 2011 over this station (see Figure 2(a) of Parihar, 2019).

Figure A1b shows derived vertical total electron content (TEC) over Hyderabad (17.3°N, 78.6°E, mlat. ~12.0°N) and Bengaluru (12.9°N, 77.6°E, mlat. ~6.7°N, formerly Bangalore), respectively, on this night (Ciraolo et al., 2007). TEC variations over Hyderabad and Bengaluru, too, show a peak in electron content around 15:40 and 17:30 UT. When correlated with the intensity peak at Ranchi, TEC peak at Hyderabad (located equatorward of Ranchi) appears afterward. Similarly, TEC peak at Bengaluru (located equatorward of Hyderabad) appears later than that at Hyderabad. As such, this equatorward moving peak in the pre-midnight hours possibly represented the EIA retreat. Global TEC maps (shown in Figures A1c and A1d) during 14:00 and 15:40 UT, too, suggest an equatorward moving TEC peak. Supported with these TEC observations and intensity variations, we interpret that the EIA retreat was active overhead.

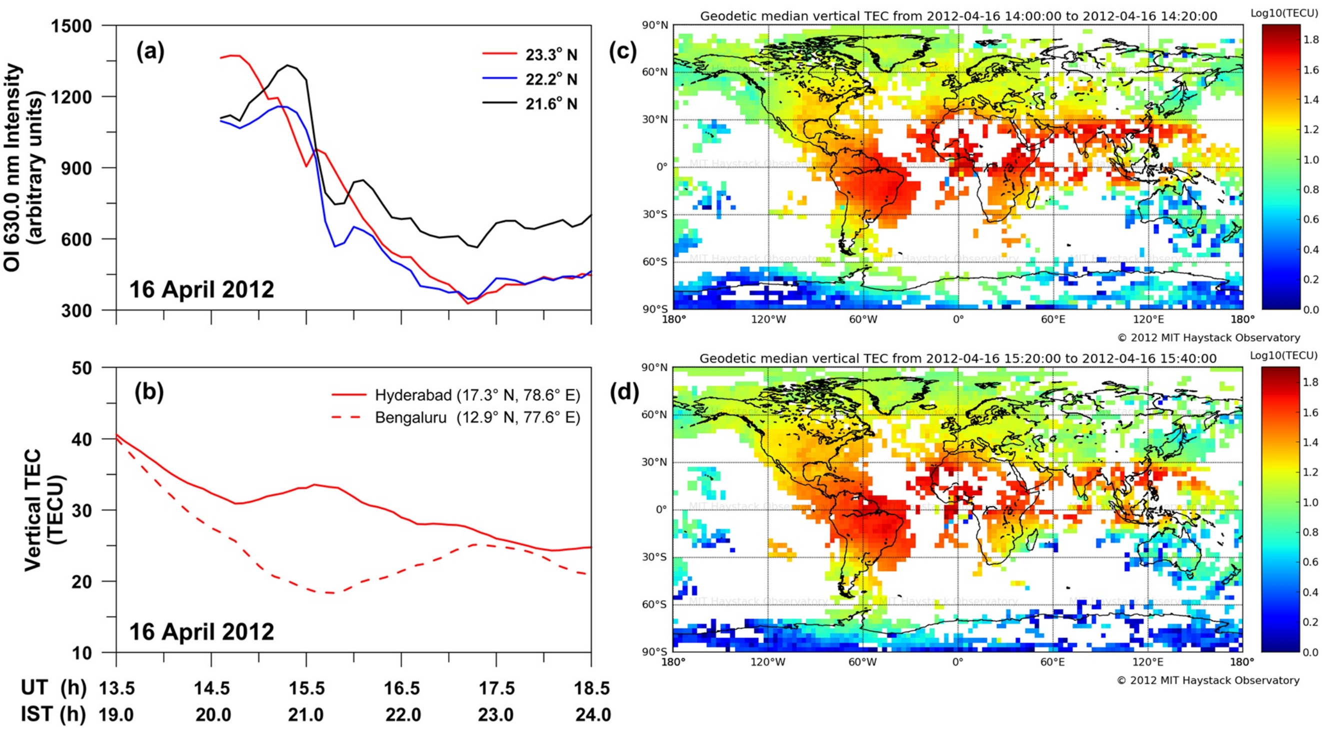

Figure A1. (a) OI 630 nm intensity variations during 14:36–18:30 UT over Ranchi showing the signatures of the equatorial ionization anomaly (EIA) retreat on 16 April 2012. Red curve shows intensity variation at ~23.3°N (which corresponds to zenith); while, blue and black curve, respectively, show intensity variation at two sample locations - 22.2°N and 21.6°N. An equatorward moving hump in intensity can clearly be seen. (b) Calibrated vertical total electron content (TEC) over Hyderabad (17.3°N, 78.6°E) (solid red curve) and Bengaluru (12.9°N, 77.6°E) (dashed red curve) showing an equatorward moving TEC peak. (c–d) Global TEC maps during 14:00–15:40 UT showing the presence of the EIA crest in the Indian subcontinent and its equatorward movement.

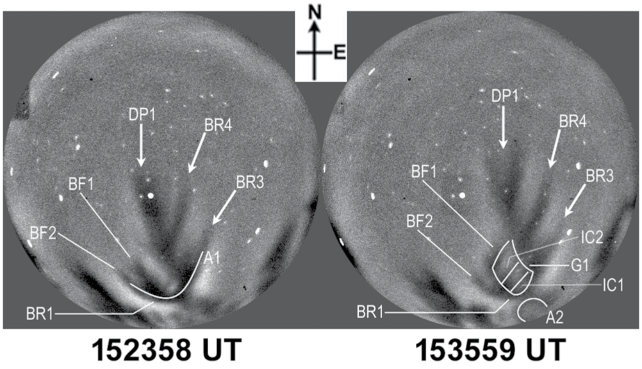

Figure B1. Selected all-sky imager 630 nm images at 15:24 UT and 15:36 UT. Starting 15:24 UT, the east wall branching BR1, the base of depletion DP1 and the west wall branching BR3 together form the cusp-shaped depleted arc, A1. At around 15:36 UT, diminished tendril TL of depletion DP1 (shown Figure 2) merged with the apex of depletion OD4 on its east and with that of small depletion SD1 on its west (both shown in Figure 2) to form an arch-shaped depletion, A2. G1 is the grid-mesh shaped feature formed by two interconnecting channels IC1, IC2 and the significantly eastward tilted bifurcation BF1 in the region between the branching BR1 and the lower fraction of depletion DP1.

Appendix B: Selected ASI 630 nm Images at 15:24 UT and 15:36 UT

Figure B1 presents the ASAI at 1524 UT and 1536 UT. Airglow image at 1524 UT shows a cusp-shaped depleted arc A1 formed by the east wall branching BR1, the base of depletion DP1 and the west wall branching BR3. Shown in airglow image at 1536 UT are (i) an arch-shaped depletion A2 formed by the merging of tendril TL with the apex of depletions OD4 and SD1 at about 1530 UT, and (ii) a grid mesh-shaped feature G1 formed by the tilted apex of bifurcation BF1, the branching BR1, two inter-connecting channels IC1 and IC2, and the lower fraction of depletion DP1.

Data Availability Statement

Airglow data used in the present study are available through the institutional data repository (http://www.iigm.res.in/) or https://doi.org/10.5281/zenodo.6926558. Calibrated TEC data was downloaded from https://t-ict4d.ictp.it/nequick2/gnss-tec-calibration (Ciraolo et al., 2007). GPS TEC data products and access through the Madrigal distributed data system are provided to the community (http://www.openmadrigal.org) by the Massachusetts Institute of Technology under support from US National Science Foundation grant AGS-1952737. Data for TEC processing is provided from the following organizations: UNAVCO, Scripps Orbit and Permanent Array Center, Institut Geographique National, France, International GNSS Service, The Crustal Dynamics Data Information System, National Geodetic Survey, Instituto Brasileiro de Geografia e Estatística, RAMSAC CORS of Instituto Geográfico Nacional de la República Argentina, Arecibo Observatory, Low-Latitude Ionospheric Sensor Network, Topcon Positioning Systems, Inc., Canadian High Arctic Ionospheric Network, Centro di Ricerche Sismologiche, Système d'Observation du Niveau des Eaux Littorales, RENAG: REseau NAtional GPS permanent, GeoNet - the official source of geological hazard information for New Zealand, GNSS Reference Networks, Finnish Meteorological Institute, and SWEPOS - Sweden. Access to these data is provided by madrigal network via: http://cedar.openmadrigal.org/.

Acknowledgments
Airglow Research at Indian Institute of Geomagnetism (http://www.iigm.res.in/) is being supported by Department of Science and Technology, Govt. of India, New Delhi (https://dst.gov.in/). We thank the editor and two reviewers for their constructive comments and recommendations that helped us to improve our manuscript.

References

Abalde, J. R., Fagundes, P. R., Bittencourt, J. A., & Sahai, Y. (2001). Observations of equatorial F region plasma bubbles using simultaneous OI 777.4 nm and OI 630.0 nm imaging: New results. *Journal of Geophysical Research*, *106*(A12), 30331–30336. https://doi.org/10.1029/2001JA001115

Ciraolo, L., Azpilicueta, F., Brunini, C., Meza, A., & Radicella, S. M. (2007). Calibration errors on experimental slant total electron content (TEC) determined with GPS. *Journal of Geodesy*, *81*(2), 111–120. https://doi.org/10.1007/s00190-006-0093-1

Fejer, B. G., & Kelley, M. C. (1980). Ionospheric irregularities. *Reviews of Geophysics*, *18*(2), 401–454. https://doi.org/10.1029/RG018i002p00401

Garcia, F. J., Kelley, M. C., Makela, J. J., Sultan, P. J., Pi, X., & Musman, S. (2000). Mesoscale structure of the midlatitude ionosphere during high geomagnetic activity: Airglow and GPS observations. *Journal of Geophysical Research*, *105*(A8), 18417–18427. https://doi.org/10.1029/1999JA000306

Guzdar, P. N., Satyanarayana, P., Huba, J. D., & Ossakow, S. L. (1982). Influence of velocity shear on the Rayleigh-Taylor instability. *Geophysical Research Letters*, *9*(5), 547–550. https://doi.org/10.1029/GL009i005p00547

Huang, C.-S., & Kelley, M. C. (1996). Nonlinear evolution of equatorial spread F: 2. Gravity wave seeding of Rayleigh-Taylor instability. *Journal of Geophysical Research*, *101*(A1), 293–302. https://doi.org/10.1029/95JA02210

Huba, J. D., & Joyce, G. (2007). Equatorial spread F modeling: Multiple bifurcated structures, secondary instabilities, large density "bite-outs," and supersonic flows. *Geophysical Research Letters*, *34*(7), L07105. https://doi.org/10.1029/2006GL028519

Hysell, D. L. (2000). An overview and synthesis of plasma irregularities in equatorial spread F. *Journal of Atmospheric and Solar-Terrestrial Physics*, *62*(12), 1037–1056. https://doi.org/10.1016/S1364-6826(00)00095-X

Kagan, L. M., & Kelley, M. C. (1998). A wind-driven gradient drift mechanism for mid-latitude E-region ionospheric irregularities. *Geophysical Research Letters*, *25*(22), 4141–4144. https://doi.org/10.1029/1998GL900123

Kelley, M. C. (2009). *The Earth's ionosphere: Plasma physics and electrodynamics* (2nd ed.). Elsevier.

Kelley, M. C., Garcia, F., Makela, J., Fan, T., Mak, E., Sia, C., & Alcocer, D. (2000). Highly structured tropical airglow and TEC signatures during strong geomagnetic activity. *Geophysical Research Letters*, *27*(4), 465–468. https://doi.org/10.1029/1999gl900598

Kelley, M. C., Larsen, M. F., LaHoz, C., & McClure, J. P. (1981). Gravity wave initiation of equatorial spread F: A case study. *Journal of Geophysical Research*, *86*(A11), 9087–9100. https://doi.org/10.1029/JA086iA11p09087

Kelley, M. C., Swartz, W. E., & Makela, J. J. (2004). Mid-latitude ionospheric fluctuation spectra due to secondary E × B instabilities. *Journal of Atmospheric and Solar-Terrestrial Physics*, *66*(17), 1559–1565. https://doi.org/10.1016/j.jastp.2004.07.004

Kil, H., Choi, H.-S., Heelis, R. A., Paxton, L. J., Coley, W. R., & Miller, E. S. (2011). Onset conditions of bubbles and blobs: A case study on 2 March 2009. *Geophysical Research Letters*, *38*(6), L06101. https://doi.org/10.1029/2011GL046885

Krall, J., Huba, J. D., Joyce, G., & Yokoyama, T. (2010). Density enhancements associated with equatorial spread F. *Annales Geophysicae*, *28*(2), 327–337. https://doi.org/10.5194/angeo-28-327-2010

Le, G., Huang, C.-S., Pfaff, R. F., Su, S.-Y., Yeh, H.-C., Heelis, R. A., et al. (2003). Plasma density enhancements associated with equatorial spread F: ROCSAT-1 and DMSP observations. *Journal of Geophysical Research*, *108*, 1318. https://doi.org/10.1029/2002JA009592

Li, Z., Lei, J., & Zhang, B. (2021). Numerical considerations in the simulation of equatorial spread F. *Journal of Geophysical Research: Space Physics*, *126*(10), e2021JA029622. https://doi.org/10.1029/2021JA029622

Makela, J. J. (2006). A review of imaging low-latitude ionospheric irregularity processes. *Journal of Atmospheric and Solar-Terrestrial Physics*, *68*(13), 1441–1458. https://doi.org/10.1016/j.jastp.2005.04.014

Makela, J. J., Kelley, M. C., & Nicolls, M. J. (2006). Optical observations of the development of secondary instabilities on the eastern wall of an equatorial plasma bubble. *Journal of Geophysical Research*, *111*(A9), A09311. https://doi.org/10.1029/2006JA011646

Martinis, C., Baumgardner, J., Mendillo, M., Su, S.-Y., & Aponte, N. (2009). Brightening of 630.0 nm equatorial spread-F airglow depletions. *Journal of Geophysical Research*, *114*(A6), A06318. https://doi.org/10.1029/2008JA013931

Martinis, C., Baumgardner, J., Smith, S. M., Colerico, M., & Mendillo, M. (2006). Imaging science at El Leoncito, Argentina. *Annales Geophysicae*, *24*(5), 1375–1385. https://doi.org/10.5194/angeo-24-1375-2006

Martinis, C., Baumgardner, J., Wroten, J., & Mendillo, M. (2018). All-sky-imaging capabilities for ionospheric space weather research using geomagnetic conjugate point observing sites. *Advances in Space Research*, *61*(7), 1636–1651. https://doi.org/10.1016/j.asr.2017.07.021

Martinis, C., & Mendillo, M. (2007). Equatorial spread F-related airglow depletions at Arecibo and conjugate observations. *Journal of Geophysical Research*, *112*(A10), A10310. https://doi.org/10.1029/2007JA012403

Mendillo, M., & Baumgardner, J. (1982). Airglow characteristics of equatorial plasma depletions. *Journal of Geophysical Research*, *87*(A9), 7641–7652. https://doi.org/10.1029/JA087iA09p07641

Mendillo, M., & Tyler, A. (1983). Geometry of depleted plasma regions in the equatorial ionosphere. *Journal of Geophysical Research*, *88*(A7), 5778–5782. https://doi.org/10.1029/JA088iA07p05778

Mukherjee, G. K. (2003). Studies of equatorial F-region depletions and dynamics using multiple wavelength nightglow imaging. *Journal of Atmospheric and Solar-Terrestrial Physics*, *65*(3), 379–390. https://doi.org/10.1016/S1364-6826(02)00214-6

Muralikrishna, P., & Vieira, L. P. (2007). Equatorial F-region irregularities generated by the Rayleigh-Taylor instability mechanism – Rocket observations from Brazil. *Revista Brasileira de Geofísica*, *25*(2), 135–149. https://doi.org/10.1590/S0102-261X2007000600016

Otsuka, Y., Shiokawa, K., Ogawa, T., & Wilkinson, P. (2002). Geomagnetic conjugate observations of equatorial airglow depletions. *Geophysical Research Letters*, *29*(15), 43-1–43-4. https://doi.org/10.1029/2002GL015347

Parihar, N. (2019). Rare occurrence of off-equatorial edge initiating and equatorward surging plasma depletions observed in OI 630-nm imaging. *Journal of Geophysical Research: Space Physics*, *124*, 2887–2896. https://doi.org/10.1029/2018JA026155

Parihar, N., Radicella, S. M., Nava, B., Migoya-Orue, Y. O., Tiwari, P., & Singh, R. (2018). An investigation of the ionospheric F region near the EIA crest in India using OI 777.4 and 630.0 nm nightglow observations. *Annales Geophysicae*, *36*(3), 809–823. https://doi.org/10.5194/angeo-36-809-2018

Parihar, N., Singh, D., & Gurubaran, S. (2017). A comparison of ground-based hydroxyl airglow temperatures with SABER/TIMED measurements over 23°N, India. *Annales Geophysicae*, *35*(3), 353–363. https://doi.org/10.5194/angeo-35-353-2017

Park, J., Stolle, C., Lühr, H., Rother, M., Su, S.-Y., Min, K. W., & Lee, J.-J. (2008). Magnetic signatures and conjugate features of low-latitude plasma blobs as observed by the CHAMP satellite. *Journal of Geophysical Research*, *113*(A9), A09313. https://doi.org/10.1029/2008JA013211

Pimenta, A. A., Fagundes, P. R., Sahai, Y., Bittencourt, J. A., & Abalde, J. R. (2003). Equatorial F-region plasma depletion drifts: Latitudinal and seasonal variations. *Annales Geophysicae*, *21*(12), 2315–2322. https://doi.org/10.5194/angeo-21-2315-2003

Pimenta, A. A., Sahai, Y., Bittencourt, J. A., & Rich, F. J. (2007). Ionospheric plasma blobs observed by OI 630 nm all-sky imaging in the Brazilian tropical sector during the major geomagnetic storm of April 6–7, 2000. *Geophysical Research Letters*, *34*(2), L02820. https://doi.org/10.1029/2006GL028529

Rastogi, R. G., & Klobuchar, J. A. (1990). Ionospheric electron content within the equatorial F2 layer anomaly belt. *Journal of Geophysical Research*, *95*(A11), 19045–19052. https://doi.org/10.1029/JA095iA11p19045

Rodrigues, F., Hickey, D., Zhan, W., Martinis, C. R., Fejer, B. G., Milla, M. A., & Arratia, J. F. (2018). Multi-instrumented observations of the equatorial F-region during June solstice: Large-scale wave structures and spread-F. *Progress in Earth and Planetary Science*, *5*(1), 14. https://doi.org/10.1186/s40645-018-0170-0

Rohrbaugh, R. P., Hanson, W. B., Tinsley, B. A., Cragin, B. L., McClure, J. P., & Broadfoot, A. L. (1989). Images of transequatorial bubbles based on field-aligned airglow observations from Haleakala in 1984-1986. *Journal of Geophysical Research*, *94*(A6), 6763–6770. https://doi.org/10.1029/JA094iA06p06763

Sahai, Y., Abalde, J. R., Fagundes, P. R., Pillat, V. G., & Bittencourt, J. A. (2006). First observations of detached equatorial ionospheric plasma depletions using OI 630.0 nm and OI 777.4 nm emissions nightglow imaging. *Geophysical Research Letters*, *33*(11), L11104. https://doi.org/10.1029/2005GL025262

10.1029/2022JA030644

Sahai, Y., Becker-Guedes, F., Fagundes, P. R., de Abreu, A. J., de Jesus, R., Pillat, V. G., et al. (2009). Observations of the F-region ionospheric irregularities in the south American sector during the October 2003 "halloween storms". *Annales Geophysicae*, *27*(12), 4463–4477. https://doi.org/10.5194/angeo-27-4463-2009

Satyanarayana, P., Guzdar, P. N., Huba, J. D., & Ossakow, S. L. (1984). Rayleigh-Taylor instability in the presence of a stratified shear layer. *Journal of Geophysical Research*, *89*(A5), 2945–2954. https://doi.org/10.1029/JA089iA05p02945

Shiokawa, K., Otsuka, Y., Ogawa, T., & Wilkinson, P. (2004). Time evolution of high-altitude plasma bubbles imaged at geomagnetic conjugate points. *Annales Geophysicae*, *22*(9), 3137–3143. https://doi.org/10.5194/angeo-22-3137-2004

Sridharan, R., Sekar, R., & Gurubaran, S. (1993). Two-dimensional high-resolution imaging of the equatorial plasma fountain. *Journal of Atmospheric and Terrestrial Physics*, *55*(13), 1661–1665. https://doi.org/10.1016/0021-9169(93)90170-4

Tsunoda, R. T. (1983). On the generation and growth of equatorial backscatter plumes: 2. Structuring of the west walls of upwellings. *Journal of Geophysical Research*, *88*(A6), 4869–4874. https://doi.org/10.1029/JA088iA06p04869

Tsunoda, R. T. (2015). Upwelling: A unit of disturbance in equatorial spread F. *Progress in Earth and Planetary Science*, *2*(1), 9. https://doi.org/10.1186/s40645-015-0038-5

Tsunoda, R. T., Livingston, R. C., McClure, J. P., & Hanson, W. B. (1982). Equatorial plasma bubbles: Vertically elongated wedges from the bottomside F layer. *Journal of Geophysical Research*, *87*(A11), 9171–9180. https://doi.org/10.1029/JA087iA11p09171

Tsunoda, R. T., & White, B. R. (1981). On the generation and growth of equatorial backscatter plumes 1. Wave structure in the bottomside F layer. *Journal of Geophysical Research*, *86*(A5), 3610–3616. https://doi.org/10.1029/JA086iA05p03610

Tsunoda, R. T., Yamamoto, M., Tsugawa, T., Hoang, T. L., Tulasi Ram, S., Thampi, S. V., et al. (2011). On seeding, large-scale wave structure, equatorial spread F, and scintillations over Vietnam. *Geophysical Research Letters*, *38*(20), L20102. https://doi.org/10.1029/2011GL049173

Wang, Z., Liu, H., Shi, J., Wang, G., & Wang, X. (2019). Plasma blobs concurrently observed with bubbles in the Asian-Oceanian sector during solar maximum. *Journal of Geophysical Research: Space Physics*, *124*(8), 7062–7071. https://doi.org/10.1029/2018JA026373

Xiong, C., Xu, J., Wu, K., & Yuan, W. (2018). Longitudinal thin structure of equatorial plasma depletions coincidently observed by Swarm constellation and all-sky imager. *Journal of Geophysical Research: Space Physics*, *123*(2), 1593–1602. https://doi.org/10.1002/2017JA025091

Yokoyama, T., Jin, H., & Shinagawa, H. (2015). West wall structuring of equatorial plasma bubbles simulated by three-dimensional HIRB model. *Journal of Geophysical Research: Space Physics*, *120*(10), 8810–8816. https://doi.org/10.1002/2015JA021799

Yokoyama, T., Shinagawa, H., & Jin, H. (2014). Nonlinear growth, bifurcation, and pinching of equatorial plasma bubble simulated by three-dimensional high-resolution bubble model. *Journal of Geophysical Research: Space Physics*, *119*(12), 10474–10482. https://doi.org/10.1002/2014JA020708

Yokoyama, T., Su, S.-Y., & Fukao, S. (2007). Plasma blobs and irregularities concurrently observed by ROCSAT-1 and Equatorial Atmosphere Radar. *Journal of Geophysical Research*, *112*(A5), A05311. https://doi.org/10.1029/2006JA012044

Zalesak, S. T., Ossakow, S. L., & Chaturvedi, P. K. (1982). Nonlinear equatorial spread F: The effect of neutral winds and background Pedersen conductivity. *Journal of Geophysical Research*, *87*(A1), 151–166. https://doi.org/10.1029/JA087iA01p00151